Synchrotron X-Ray Study of Lung Surfactant-Specific Protein SP-B in Lipid Monolayers

Ka Yee C. Lee,* Jaroslaw Majewski,† Tonya L. Kuhl,‡ Paul B. Howes,§ Kristian Kjaer,§ Michael M. Lipp,¶ Alan J. Waring,‖ Joseph A. Zasadzinski,‡ and Greg S. Smith†

*Department of Chemistry and Institute for Biophysical Dynamics, The University of Chicago, Chicago, Illinois 60637 USA; †Manuel Lujan Jr. Neutron Scattering Center, Los Alamos National Laboratory, Los Alamos, New Mexico 87545 USA; ‡Department of Chemical Engineering, University of California, Santa Barbara, California 93106 USA; §Condensed Matter Physics and Chemistry Department, Risø National Laboratory, DK-4000, Roskilde, Denmark; ¶Advanced Inhalation Research/Alkermes, Cambridge, Massachusetts 02139 USA; and ‖Department of Pediatrics, Martin Luther King Jr./Drew Medical Center and University of California, Los Angeles, Los Angeles, California 90095 USA

ABSTRACT This work reports the first x-ray scattering measurements to determine the effects of SP-B_{1-25}, the N-terminus peptide of lung surfactant-specific protein SP-B, on the structure of palmitic acid (PA) monolayers. In-plane diffraction shows that the peptide fluidizes a portion of the monolayer but does not affect the packing of the residual ordered phase. This implies that the peptide resides in the disordered phase, and that the ordered phase is essentially pure lipid, in agreement with fluorescence microscopy studies. X-ray reflectivity shows that the peptide is oriented in the lipid monolayer at an angle of ~56° relative to the interface normal, with one end protruding past the hydrophilic region into the fluid subphase and the other end embedded in the hydrophobic region of the monolayer. The quantitative insights afforded by this study lead to a better understanding of the lipid/protein interactions found in lung surfactant systems.

INTRODUCTION

A complex mixture of lipids and proteins, known as lung surfactant (LS), is secreted by type II pneumocytes lining the alveoli and is essential for proper lung function (Shapiro and Notter, 1989). LS lowers the surface tension as the alveolar volume decreases, which reduces the work of breathing and stabilizes the alveoli against collapse. To achieve low surface tensions, LS must adsorb rapidly to the air-fluid interface of the alveoli after being secreted. Once at the interface, LS forms a monolayer that can vary the surface tension as a function of the alveolar radius. The minimum surface tension that can be achieved by a given monolayer is set by a two- to three-dimensional instability known as monolayer collapse, which occurs when the surface area of the monolayer is reduced past a critical value. A good lung surfactant should resist collapse; however, should collapse occur due to over-compression during exhalation, the collapsed monolayer should still be able to respread rapidly on expansion. Inadequate surfactant, due to either immaturity in premature infants, or disease or trauma in adults, can result in respiratory distress syndrome (RDS), a potentially lethal disease in both populations. In infants, RDS can be treated by administration of synthetic or naturally derived replacement surfactants (Shapiro and Notter, 1989). Design of such surfactants is largely empirical due to a lack of basic understanding of the roles of the individual components of LS, the way these components interact in the monolayer, and the way the components collectively affect monolayer collapse and respreading.

Endogenous LS is a complex, multicomponent mixture, the precise composition of which is still not completely defined (Johansson and Curstedt, 1997). LS consists primarily (40–50 wt %) of saturated dipalmitoylphosphatidylcholine (DPPC) and smaller fractions of unsaturated phosphatidylcholines (PCs), anionic phospholipids such as phosphatidylglycerols (PGs), anionic lipids like palmitic acid (PA), and neutral components like cholesterol (Keough, 1985; Shapiro and Notter, 1989; Veldhuizen et al., 1998). LS also contains four lung surfactant-specific proteins, known as SP-A, -B, -C, and -D (Possmayer, 1988). SP-A and SP-D are larger proteins responsible for host-defense mechanisms as well as the transport and recycling of LS, whereas SP-B and SP-C are smaller, amphipathic proteins important to surface activity. Although the complete roles of SP-B and SP-C are not yet fully understood, they are essential for proper LS function in vivo and in replacement surfactants for the treatment of RDS. SP-B, in particular, has been shown to greatly increase the beneficial function of LS lipids both in vitro and in vivo (Mizuno et al., 1995; Tokieda et al., 1997; Walther et al., 1997; Walther et al., 1998) and plays important roles in clinical surfactants (Hall et al., 1992). In earlier work by some of us, it was shown that simple peptide sequences based on the amino terminus of SP-B possess similar activity as the native protein (Waring et al., 1989; Takahashi et al., 1990; Gordon et al., 1996; Lipp et al., 1996).

Pure DPPC forms monolayers that resist collapse to high surface pressure (~70 mN/m). However, under physiological conditions the adsorption from solution and respreading

Received for publication 11 December 2000 and in final form 18 April 2001.

T. L. Kuhl's present address: Department of Chemical Engineering and Materials Science, University of California, Davis, CA 95616.

Address reprint requests to Dr. Ka Yee C. Lee, Department of Chemistry, The University of Chicago, 5735 S. Ellis Avenue, Chicago, IL 60637. Tel.: 773-702-7068; Fax: 773-702-0805; E-mail: kayeelee@uchicago.edu.

0006-3495/01/07/572/14 $2.00

of DPPC is slow, rendering it unsuitable as a replacement LS candidate (Shapiro and Notter, 1989; Mathialagan and Possmayer, 1990; Cockshutt et al., 1991; Longo et al., 1992). The unsaturated and anionic lipids present in natural LS are believed to enhance the adsorption and respreading of DPPC (Mathialagan and Possmayer, 1990; Cockshutt et al., 1991; Longo et al., 1992). In particular, PA is one of the three compounds added to exogenous surfactant in Survanta (8.5 w/w; Ross Laboratory, Columbus, OH) and Surfactant TA (8.5% w/w; Tokyo Tanabe, Tokyo, Japan) used to treat premature infants with neonatal RDS. However, PA has a low collapse pressure relative to DPPC (as do most of the anionic and unsaturated components of LS), leading to the idea that LS monolayers are refined by the selective removal of lipids with low collapse pressures on repeated compression and expansion, a phenomenon known as squeeze-out (Cockshutt et al., 1991; Pastrana-Rios et al., 1994). There is evidence that some unsaturated lipid components of LS are squeezed out of binary monolayers containing DPPC or dipalmitoylphosphatidylglycerol (DPPG) (Egbert et al., 1989; Cockshutt et al., 1991). However, these experiments have neglected the effects of LS proteins on monolayer behavior. In fact, LS lipids and proteins act synergistically to remove the driving force for squeeze-out of the fluidizing components (Lipp et al., 1996, 1998). The addition of full-length SP-B or its amino-terminus peptide, SP-$B_{1–25}$, to monolayers of PA or PGs results in much higher monolayer collapse pressures (lower collapse surface tension values) than those of either lipid or protein alone (Lipp et al., 1996, 1998). This suggests that interactions between PA and SP-B may result in the retention of both the lipid and the protein in the monolayer upon compression (Longo et al., 1992).

Optical microscopy and isotherm measurements have shown that human lung surfactant protein SP-B and its amino terminus, SP-$B_{1–25}$, alter the phase behavior of palmitic acid monolayers by creating a new fluid protein-rich phase. This fluid phase forms a network that separates condensed-phase domains at coexistence and persists to high surface pressures. The network changes the monolayer collapse mechanism from heterogeneous nucleation and growth (on pure water subphases) or irreversible fracturing (on buffered saline subphases) to a homogeneous nucleation process by isolating individual condensed-phase domains (Lipp et al., 1996, 1997; Lee et al., 1997). This results in higher surface pressure at collapse. In addition, the collapse structures are much smaller, and hence the monolayer is easier to respread on expansion, factors essential to the in vivo function of lung surfactant. Formation of a protein-rich fluid phase is also crucial to enhanced performance in phosphatidylglycerol monolayers with SP-B (Lipp et al., 1998). Although isotherms and fluorescence imaging provide qualitative information on the PA/SP-B interactions, quantitative data on these interactions and on the location of the protein in the monolayer require a molecular scale probe such as x-ray diffraction and reflectivity.

It is only with the advent of intense and well collimated x-ray beams from synchrotron sources that it has become possible to obtain direct structural information on the organization of amphiphilic molecules at the air-water interface via surface x-ray scattering methods (Als-Nielsen et al., 1994; Kaganer et al., 1999). We present a series of x-ray grazing-incidence diffraction (GIXD) and reflectivity (XR) experiments from both pure PA and mixed PA/SP-$B_{1–25}$ monolayers at the air-fluid interface at different temperatures, on different subphases, and at different surface pressures. The resulting diffraction and reflectivity data give us the first quantitative information on the effect of SP-$B_{1–25}$ on the packing of the PA monolayer and on monolayer collapse, and help to pinpoint the location of the peptide in the lipid matrix.

MATERIALS AND METHODS

Materials

Palmitic acid (PA; Sigma Chemical Co., St. Louis, MO; >99% pure) was used as obtained. All subphases were prepared using 18.2 MΩ · cm Millipore water obtained from a Milli-Q UV Plus system (Bedford, MA). Physiological subphases contained 0.15 M NaCl and a 2 mM $NaHCO_3$ buffer (pH = 6.9). Stock spreading solutions were made with either pure chloroform (for PA) or 4:1 v/v chloroform-methanol (for SP-$B_{1–25}$). Spreading solutions were made by mixing aliquots of the stock solutions to obtain the desired lipid/protein concentration.

The synthetic peptide based on the first 25 amino acids of the NH_2-terminal sequence of SP-B, SP-$B_{1–25}$, shown in Fig. 1, was prepared using an Applied Biosystems (Foster City, CA) 431A peptide synthesizer and purified as described previously (Gordon et al., 1996). The expected molecular mass for SP-$B_{1–25}$ was obtained by fast atom bombardment mass spectrometry (UCLA Center for Molecular and Medical Mass Spectrometry, Los Angeles, CA). Quantitative amino acid composition for the peptide was determined at the UCLA Protein Microsequencing Facility.

Experimental configuration

All synchrotron x-ray measurements were performed with the liquid surface diffractometer (Als-Nielsen and Kjaer, 1989; Majewski et al., 1995) at the BW1 (undulator) beam line (Frahm et al., 1995) at HASYLAB, DESY (Hamburg, Germany). A thermostatted Langmuir trough, equipped with a Wilhelmy balance for measuring the surface pressure (π), and a barrier for surface pressure control, was mounted on the diffractometer. In a typical experiment, a monolayer of PA or PA with 20 wt % SP-$B_{1–25}$ was first spread at the desired temperature using a microsyringe. At least 30 min were allowed for complete solvent evaporation before the two-dimensional film was compressed to the desired surface pressure. The film was then held at this surface pressure throughout the experiment. The trough was enclosed in a sealed, helium-filled canister where the oxygen level was constantly monitored.

FIGURE 1 Amino acid sequence of the truncated model peptide SP-$B_{1–25}$, with the positively charged residues indicated by plus signs.

The synchrotron x-ray beam was monochromated to a wavelength of $\lambda \sim 1.303$ Å by Laue reflection from a Be (200) monochromator crystal. By tilting the reflecting planes out of the vertical plane, the monochromatic beam could be deflected down to yield a glancing angle with the horizontal liquid surface.

For the GIXD experiments, the x-ray beam was adjusted to strike the surface at an incident angle of $\alpha_i = 0.11° = 0.85\ \alpha_c$, where α_c is the critical angle for total external reflection. At this angle the incident wave is totally reflected, whereas the refracted wave becomes evanescent, traveling along the liquid surface. Such a configuration maximizes surface sensitivity (Eisenberger and Marra, 1981). The dimensions of the incoming x-ray beam footprint on the liquid surface were ~5 mm × 50 mm or 1 mm × 50 mm.

For XR measurements, a set of slits was used to exclude diffuse scattered background around the reflected beam. These slits, along with a scintillation detector, were mounted on an elevator. The absolute reflectivity was derived by subtracting the measured background and normalizing to the incident flux. For GIXD measurements, the post-sample slits were replaced by a Soller collimator with vertical plates, giving a horizontal resolution, $\Delta Q_{xy} = 0.0075$ Å^{-1}. The scintillation counter was replaced by a vertical one-dimensional position sensitive detector (PSD) with vertical acceptance $0 < Q_z < 0.9$ Å^{-1}, allowing Bragg rod measurements to be made. A schematic of the experimental geometry and the experimental setup is shown in Fig. 2.

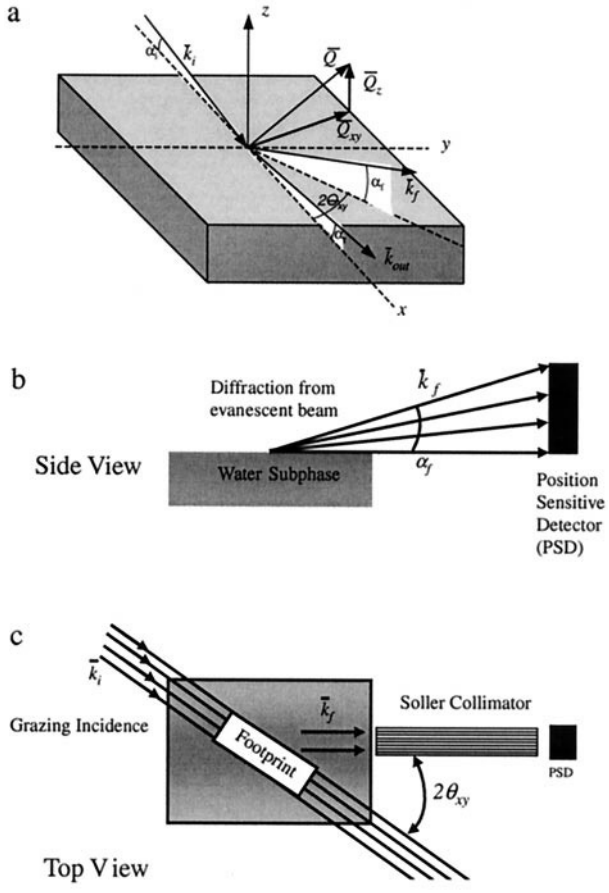

FIGURE 2 Schematics of the experimental setup and geometry for both XR and GIXD measurements. (*a*) Overall view; (*b*) Side view; (*c*) Top view. The wavevector k has length $|k| = 2\pi/\lambda$. For XR, $\alpha_r = \alpha_i = \alpha$, and $Q_z = 2k \sin\alpha$, $Q_{xy} = 0$. For GIXD, $Q_z = k(\sin\alpha_i + \sin\alpha_f) \sim k \sin\alpha_f$ and $Q_{xy} \sim 2k \sin(2\theta_{xy}/2)$ (Weissbuch et al., 1997).

In three-dimensional (3D) crystals, Bragg diffraction takes place only when the scattering vector Q coincides with the $\{h, k, l\}$ points of the reciprocal 3D lattice, giving rise to Bragg spots (h, k, l are the Miller indices). In our two-dimensional (2D) systems and at surface pressures of interest, the PA monolayers are a mosaic of 2D crystals with random orientation about the direction normal to the subphase and can therefore be described as 2D powders. Due to the lack of a vertical crystalline repeat, there is no restriction on the scattering vector component Q_z along the direction normal to the crystal: Bragg scattering from a 2D crystal extends as continuous Bragg rods through the reciprocal space (Als-Nielsen and Kjaer, 1989; Als-Nielsen et al., 1994; Kjaer, 1994). The scattered intensity is measured by scanning over a range of horizontal scattering vectors $Q_{xy} \sim (4\pi/\lambda)\sin(2\theta_{xy}/2)$, where $2\theta_{xy}$ is the angle between the incident and diffracted beam (see Fig. 2). The Bragg peaks, resolved in the Q_{xy} direction, are obtained by integrating the scattered intensity over all the channels along the Q_z direction in the PSD. Conversely, the Bragg rod profiles are obtained by integrating, after background subtraction, for each PSD channel, the scattered intensity across a Bragg peak. The angular positions of the Bragg peaks allow the determination of the spacings $d = 2\pi/Q_{xy}$ for the 2D lattice. From the line shapes of the peaks, it is possible to determine the 2D crystalline coherence length L (the average distance in the direction of the reciprocal lattice vector Q_{xy} over which crystallinity extends). The intensity distribution along the Bragg rod can be analyzed to determine the direction and magnitude of the molecular tilt, the out-of-plane coherence length L_c, and the magnitude of molecular motion or surface roughness of the crystallite (Debye-Waller factor).

Detailed information on the electron density distribution in the direction normal to the interface, averaged laterally over both the ordered and disordered parts of the film, can be determined by modeling the deviation of the measured specular x-ray reflectivity from Fresnel's law for a perfect interface. In our analysis, a slab model was used in which the monolayer was represented as a stack of slabs, with each slab having a constant electron density and thickness. The interfaces between slabs were smeared out with Gaussian function of standard deviation σ to account for roughening at the boundary due to static or thermal roughness of the interface (Als-Nielsen and Kjaer, 1989; Als-Nielsen et al., 1994).

RESULTS

Experiments were carried out at 16°C on a pure water subphase and at 25°C on a buffered saline subphase. On pure water, 16°C is well below the triple point of a PA monolayer (Lipp et al., 1996, 1997). The triple point denotes the unique temperature and surface pressure in the pure component phase diagram where the condensed (LC), liquid-expanded (LE), and gaseous (G) phases all coexist in equilibrium. As the LE phase does not exist below the triple-point temperature, a LC film is guaranteed at low non-zero surface pressures. These conditions thus made it possible to probe any fluidizing effect of the peptide on the PA monolayer. For the second set of experiments, a buffered saline subphase (0.15 M NaCl in a 2 mM $NaHCO_3$ buffer, pH 6.9) was used to be representative of physiological conditions. The temperature of 25°C is well above the triple point of PA, so the system undergoes G → LE → LC → solid condensed phase transitions before collapsing.

Within each series, both GIXD and XR measurements were made on pure PA as well as mixed PA/20 wt % SP-B_{1-25} monolayers, with the films held at different surface pressures. The lipid/peptide ratio was chosen to mimic that of PA and SP-B found in natural LS. In all cases, the

pure PA experiments gave a baseline for comparison with the mixed monolayer. We have also examined collapse structures of films in the presence and the absence of SP-$B_{1–25}$ under identical subphase and temperature conditions.

Pure water subphase at 16°C

Grazing incidence x-ray diffraction on pure PA

The diffraction pattern obtained for pure PA monolayers at $\pi = 15$ mN/m and $\pi = 30$ mN/m are shown in Fig. 3 *a*. At $\pi = 15$ mN/m, two Bragg peaks are observed at $Q_{xy} = 1.45$ Å^{-1} and $Q_{xy} = 1.50$ Å^{-1}; the corresponding coherence lengths are 160 Å and 450 Å, respectively. The observation of precisely two Bragg peaks in the 2D powder pattern is indicative of a rectangular unit cell (Jacquemain et al., 1991). Previous work on fatty acid monolayers has also shown that in the rectangular *S*, *L2*, *L2′* phases these monolayers yield two in-plane reflections: $\{1,1\}_{rect}$ and $\{0,2\}_{rect}$ (unit cell shown in Fig. 3 *c* on the right) (Kjaer et al., 1989; Lin et al., 1990; Kenn et al., 1991; Kaganer et al., 1999). The integrated intensity of the Bragg peak at $Q_{xy} = 1.45$ Å^{-1} peak is roughly twice that of the $Q_{xy} = 1.50$ Å^{-1} peak. This higher intensity results from coincident $\{1,1\}_{rect}$ and $\{1,-1\}_{rect}$ reflections and thus leads to the assignment of the $\{1,1\}_{rect}$ reflection to the $Q_{xy} = 1.45$ Å^{-1} peak and the $\{0,2\}_{rect}$ reflection to the $Q_{xy} = 1.50$ Å^{-1} peak. The calculated *d*-spacings, $d_{11} = 4.33$ Å ($d_{xy} = 2\pi/Q_{xy}$) and $d_{02} = 4.19$ Å, give rise to a rectangular unit cell with axes $|a| = 5.06$ Å ($1/|a|^2 = (1/d_{11}^2 - 1/(2d_{02})^2)$ and $|b| = 8.38$ Å, and an area per chain, A_{15}, of 21.2 Å^2 (two molecules per unit cell of area = 42.4 Å^2).

The Bragg rod profiles for the two reflections are shown in Fig. 4. The $\{0,2\}_{rect}$ Bragg rod has its maximum in the intensity profile at $Q_z \sim 0$ Å^{-1}, which indicates that the molecular axis lies in a plane perpendicular to the *b* axis. We analyzed the $\{1,1\}_{rect}$ and $\{0,2\}_{rect}$ Bragg rod intensity profiles by approximating the PA molecule by a cylinder with constant electron density (Als-Nielsen and Kjaer, 1989). Our results show that the molecule has a tilt of ~21° toward the nearest neighbor (along unit vector *a*) direction, and the effective thickness (thickness projected on the surface normal) of the monolayer is 20.5 Å.

When the system is compressed to 30 mN/m, the two Bragg peaks at 15 mN/m collapse into one (see Fig. 3 *a*), indicating a transition to a hexagonal lattice (see Fig. 3 *c*). The scattering vector for the single Bragg peak, indexed as $\{1,0\}_{hex}$ (unit cell shown in Fig. 3 *c* on the left) is $Q_{xy} =$

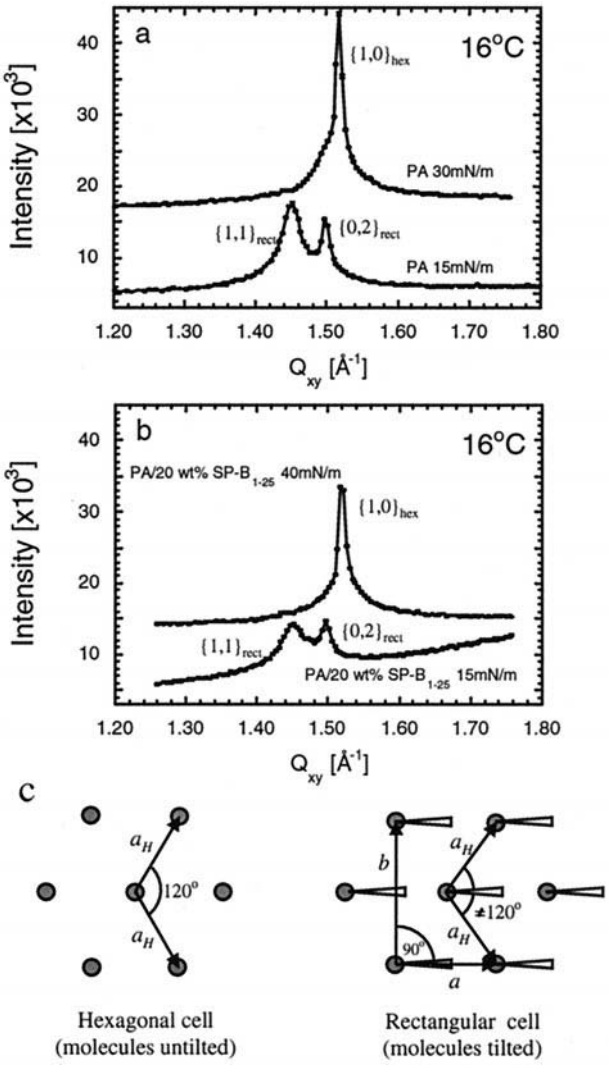

FIGURE 3 Bragg peaks from GIXD on pure water at 16°C. (*a*) Pure PA film at 15 mN/m and 30 mN/m; (*b*) Mixed PA/20 wt % SP-$B_{1–25}$ film at 15 mN/m and 40 mN/m. For clarity, the high-pressure data have been offset vertically. (*c*) Diagrams from above showing a hexagonal cell with untilted molecules and a rectangular cell with tilted molecules, represented by triangles tilting toward the *a* direction.

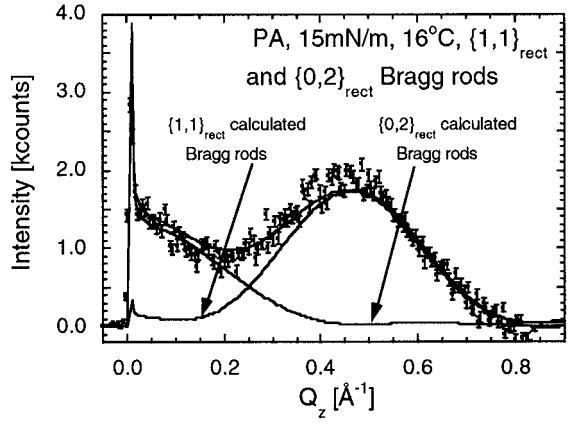

FIGURE 4 Bragg rod profiles for Bragg rods in the $\{1,1\}_{rect}$ and $\{0,2\}_{rect}$ directions for a pure PA film on water subphase at 16°C and 15 mN/m. The rods were fitted (——) by approximating the coherently scattering part of the fatty acid tail by a cylinder of constant electron density.

1.52 $Å^{-1,}$ with an average coherence length of 470 Å, which is a significant increase over the coherence length of the $\{1,1\}_{rect}$ reflections at 15 mN/m. The hexagonal lattice has a *d*-spacing of 4.13 Å, and the unit cell dimension (an intermolecular distance) $a_H = d/\cos 30° = 4.77$ Å. The interfacial area per chain, A_{30}, is reduced to 19.7 $Å^2$. The position of the intensity maximum of the Bragg rod ($Q_z \sim 0$ $Å^{-1}$; data not shown) implies ~0° tilt of the molecules.

Using areas obtained for surface pressures of 15 mN/m (A_{15}) and 30 mN/m (A_{30}), we find once again the tilt angle of the chain at 15 mN/m, $t_{15} = \arccos(A_{30}/A_{15}) \sim 21°$. These results agree very well with those obtained from the fits to the $\{1,1\}_{rect}$ and $\{0,2\}_{rect}$ Bragg rods (Fig. 4, solid lines). The quantitative information shows that an increase in surface pressure primarily causes a decrease in the area per PA molecule due to a decrease in molecular tilt, while maintaining the molecular packing in the plane normal to the molecules.

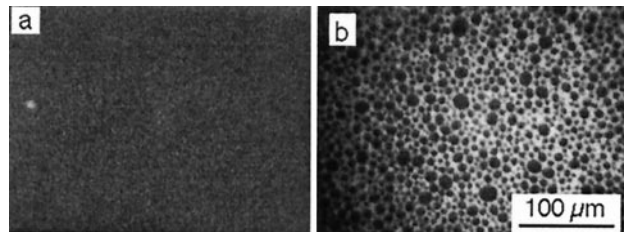

FIGURE 5 Fluorescence micrographs of a pure PA film (*a*) and a mixed PA/20 wt % SP-$B_{1–25}$ film (*b*) at 16°C on a pure water subphase at the lift-off point. All mixtures contain less than 1 mol % (with respect to the PA concentration) of the fluorescent probe, *N*-7-nitrobenz-2-oxa-1,3-diazol-4-yl-hexadecylamine. As 16°C is below the triple point of PA, the pure PA film exhibits a uniform condensed phase at non-zero surface pressures (*a*). The addition of SP-$B_{1–25}$ to the PA film inhibits the formation of the condensed phase, leading to the formation of a disordered, bright fluid phase that separates the remaining condensed-phase domains (*b*). The image contrast results from the exclusion of the dye from the more ordered, condensed phases (dark) and its incorporation in the more disordered, expanded phases (bright).

Grazing incidence x-ray diffraction on PA/20 wt % SP-$B_{1–25}$

The Bragg peaks obtained for the lipid/peptide mixed monolayers at 15 mN/m and 40 mN/m are shown in Fig. 3 *b*. At 15 mN/m, two Bragg peaks resulting from $\{1,1\}_{rect}$ and $\{0,2\}_{rect}$ reflections are observed at $Q_{11} = 1.45$ $Å^{-1}$ and $Q_{02} = 1.50$ $Å^{-1}$, with coherence lengths $L_{11} = 130$ Å and $L_{02} = 425$ Å. The *d*-spacings have values $d_{11} = 4.33$ Å and $d_{02} = 4.20$ Å, indicating a rectangular unit cell with axes $|a| = 5.05$ Å and $|b| = 8.40$ Å with an interfacial area per molecule of 21.2 $Å^2$. Similar to the pure PA case, the $\{0,2\}_{rect}$ Bragg rod has its maximum intensity at $Q_z \sim 0$ $Å^{-1}$, and the profile of the $\{1,1\}_{rect}$ reflection gives a tilt angle of 20.4° toward the nearest neighbor (along unit vector *a*) direction. Comparing these results with those for pure PA, it is apparent that the presence of SP-$B_{1–25}$ does not affect the lipid packing of the condensed phase. The unit cell, the coherence lengths, and the molecular tilt found in the condensed phase of PA are all preserved in this mixed system. This suggests that the peptide is completely excluded from the condensed region of the film, consistent with fluorescence imaging (see Fig. 5) (Lipp et al., 1996, 1997). As a PA monolayer at 16°C is well below the triple point and should be in a pure LC phase at 15 mN/m, our results indicate that incorporating the peptide into the monolayer creates a disordered phase whose structure cannot be probed by the GIXD techniques.

Corroborative evidence of this disordered phase can be found by the drop (by a factor of ~2.1) in integrated intensity observed when SP-$B_{1–25}$ is present (see Fig. 3, *a* and *b*). Because GIXD is sensitive only to the ordered phase, this decrease in scattering intensity suggests that a disordered phase occupies ~50% of the monolayer surface area, which is qualitatively consistent with our fluorescence microscopy findings (see Fig. 5) (Lipp et al., 1996, 1997).

At 40 mN/m, the mixed film exhibits a single Bragg peak at $Q_{xy} = 1.52$ $Å^{-1}$ with a coherence length of 450 Å. As was observed without the peptide, the condensed phase of the monolayer assumes a hexagonal packing with ~0° molecular tilt. The *d*-spacing is 4.13 Å, with an intermolecular separation of 4.77 Å and an area per molecule of 19.8 $Å^2$. These lattice parameters are identical (within experimental errors) to the pure PA monolayers at 30 mN/m. This implies that the condensed phase of the film at this elevated pressure is made up only of PA molecules. A direct comparison at 40 mN/m is not possible because the pure PA film collapses below 40 mN/m. Unlike the low-surface-pressure case, the integrated intensity found in this case is only slightly lower than that in pure PA at 30 mN/m, the ratio being ~1.3. It should be noted that the two cases are at different pressures (30 mN/m without protein; 40 mN/m with protein), which may also account for the smaller decrease in the scattering intensity. Nonetheless, the smaller decrease is consistent with fluorescence images that show a smaller fluid phase at higher surface pressures (Lee et al., 1997; Lipp et al., 1997).

X-ray reflectivity

The x-ray reflectivity data for a pure PA monolayer at 15 mN/m are shown in Fig. 6 *a*. At 15 mN/m and 16°C, only the LC phase exists. A two-box model was used to fit the data (see Fig. 6 *a′*), with one box representing the electron density of the COOH headgroup, and the second box representing the electron density of the tail. Both boxes were convoluted with a Gaussian smearing function of standard deviation σ to account for the roughness of the monolayer at the air-water interface. The fitting was carried out with all parameters free except the number of electrons in the tail (fixed at 121, corresponding to the tail portion, $CH_3(CH_2)_{14}$,

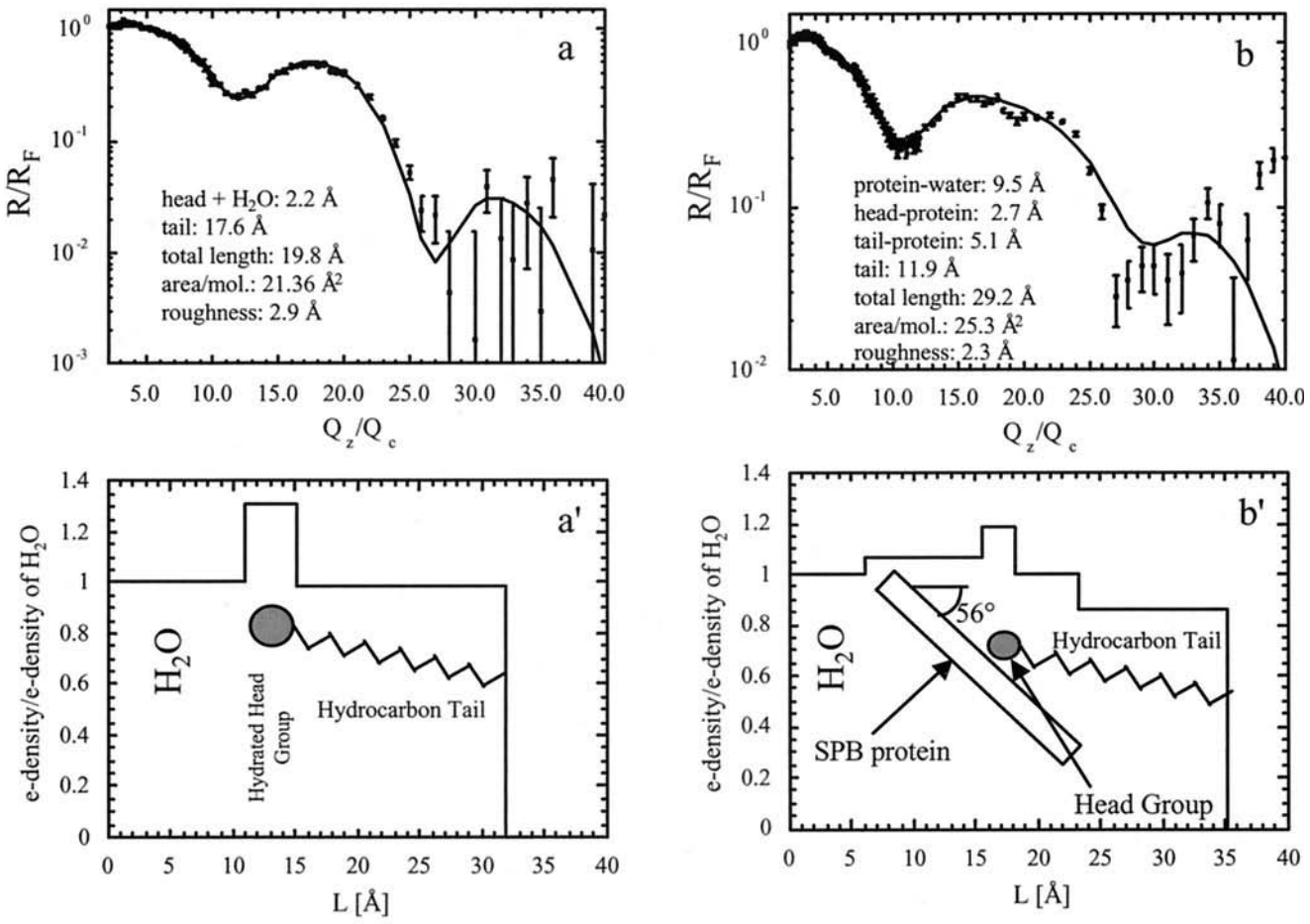

FIGURE 6 X-ray reflectivity data and fits for a pure PA monolayer at 15 mN/m (*a*) and a mixed PA/SP-B_{1-25} monolayer at 40 mN/m (*b*). (*a′*) A two-box model is used for the pure PA film; (*b′*) A four-box model for the mixed lipid/peptide system. The fitted parameters are shown in *a* and *b*.

of the palmitic acid molecule). The fit gives an area per molecule of 21.4 $Å^2$ and a thickness of the hydrocarbon layer of 17.6 Å, resulting in a molecular tilt of 21.5° and a total film thickness of 19.8 Å. These values are in good agreement with the GIXD results described above.

For PA/SP-B_{1-25} at 40 mN/m, Fig. 6 *b* shows the reflectivity curve for the mixed lipid/peptide monolayer at 16°C. The best fit to the data was obtained using a four-box model (Fig. 6 *b′*), with the boxes representing the electron density of 1) the portion of the peptide protruding into the subphase, 2) the headgroup with a portion of the peptide, 3) part of the tail region with a portion of the peptide, and 4) the remaining tail portion. Again the model was convoluted with a Gaussian smearing function of standard deviation σ. The fitting parameters are listed in Fig. 6 *b* and Table 1. The fit gives a total thickness of the peptide-PA layer of 29.2 Å, with one end of the peptide protruding into the water subphase, and the other end embedded within the tail region. Within this peptide-PA layer, the peptide occupies a portion that measures 17.3 Å in thickness. A recent molecular dynamic simulation study on SP-B_{1-25} gives an average length of the molecule of 31 Å (Gordon et al., 2000). The entire atomic coordinate set for SP-B_{1-25} can be found in the National Institutes of Health/National Science Foundation-sponsored Protein Data Bank (PPD access code 1DFW). This dimension accounts for both the sheet at the N-termi-

TABLE 1 Fitting parameters for XR data on pure water at 16°C

	Thickness (Å)	Electron density ρ (number of electrons)	Area/ molecule	Roughness σ
PA			21.36	2.9
Tail	17.6	0.96 (121)		
Head	2.2	1.53 (24)		
PA with SP-B_{1-25}			25.3	2.3
Tail	11.9	0.87 (87)		
Tail-protein	5.1	1.0 (43)		
Head-protein	2.7	1.18 (27)		
Protein-water	9.5	1.06 (85)		

All electron densities are normalized by the electron density of water ($\rho_{water} = 0.334e^-/Å^3$).

nus as well as the center helical portion of the peptide, but neglects the last three residues, which constitute the "run" at the C-terminus. Because it is the N-terminus of the peptide that is responsible for the insertion (Gordon et al., 1996; Hawgood et al., 1998), our results indicate that the average molecular axis of the peptide inserts into the lipid monolayer at an angle of ~56° with respect to the air-water interface normal (see Fig. 7).

The GIXD results on the system show that there exists an ordered phase made up of PA with the molecular axes approximately normal to the interface and that the peptide is incorporated in a disordered phase with PA. Unlike GIXD, XR measurements are sensitive to both the crystalline and non-crystalline phases. If the disordered phase disappears at this elevated surface pressure, the film should then consist only of an ordered phase, and the reflectivity data should be fitted using a two-box model. However, attempts to fit with a two-box and even a three-box model resulted in poor fits with very large χ^2 values, suggesting that the peptide-enriched disordered phase exists at elevated surface pressures. Fitting with the four-box model gives an average molecular area of 25.3 Å^2. It should be noted that the four-box model fit performed here gives the average configuration of the monolayer by taking into account both the ordered and disordered phases, thus resulting in an average area that is greater than that obtained using GIXD (only ordered phase detected). A discussion on incoherent versus coherent averaging of the x-ray reflectivity data is included in the Appendix.

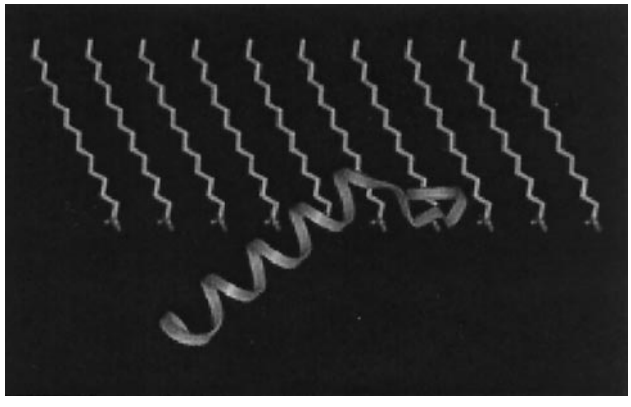

FIGURE 7 Molecular graphics representation of SP-$B_{1–25}$ in the PA monolayer at a surface pressure of 30 mN/m. Green stick structures represent PA; the ribbon structure represents a SP-$B_{1–25}$ peptide derived from molecular simulation of isotope-enhanced FTIR measurements of the molecule in a lipid environment, with the N-terminus of the peptide inserting into the lipid layer. The PA molecules are tilted and spaced at 5 Å, and the peptide average molecular axis is oriented at an angle of 56° relative to surface normal.

Buffered saline subphase at 25°C

Grazing incidence x-ray diffraction on pure PA

Fig. 8 shows a single hexagonal $\{1,0\}_{hex}$ Bragg peak at Q_{xy} = 1.50 Å^{-1} from a pure PA film at 30 mN/m. The coherence length is 560 Å. The $Q_z \sim 0$ Å^{-1} location (data not shown) for the maximum of the Bragg rod intensity suggests that the molecular axis is normal to the water surface. The *d*-spacing of 4.19 Å gives a hexagonal unit cell dimension a_H of 4.84 Å and an area per molecule of 20.3 Å^2. Compared with a similar film on pure water at 16°C, the coherence length is longer despite the higher temperature, and the molecular area is slightly larger, probably as a result of the increased temperature.

Grazing incidence x-ray diffraction on PA/20 wt % SP-$B_{1–25}$

The same single Bragg peak at Q_{xy} = 1.50 Å^{-1} at 30 mN/m (see Fig. 8) was obtained for mixed films of PA and 20 wt % SP-$B_{1–25}$. From the *d*-spacing of 4.20 Å, the hexagonal unit cell dimension a_H is 4.85 Å, with the area per molecule of 20.3 Å^2. All these parameters are essentially identical to those obtained for the pure PA monolayer, indicating that the ordered phase in the mixed film is exclusively made up of PA molecules. Again this suggests that the peptide resides only in the disordered phase of the monolayer. The integrated intensity decreases by a factor of ~1.7 when SP-$B_{1–25}$ is present in the film (see Fig. 8), further indicating that the presence of the peptide leads to a higher area fraction of the disordered phase in the surface film. The coherence length in the mixed film is 350 Å, which is a significant reduction from the 560-Å value found in the pure PA film. This again is consistent with our fluorescence microscopy observation that the peptide disrupts the ordered

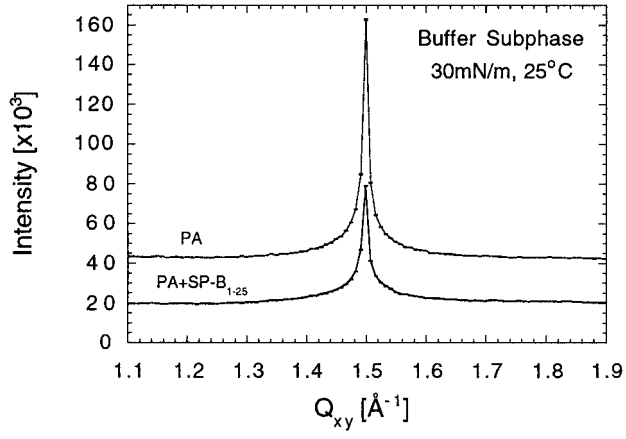

FIGURE 8 Bragg peaks from GIXD on buffered saline subphase at 25°C of a pure PA and a mixed PA/20 wt % SP-$B_{1–25}$ films, both at a surface pressure of 30 mN/m. For clarity, the pure PA data have been offset vertically.

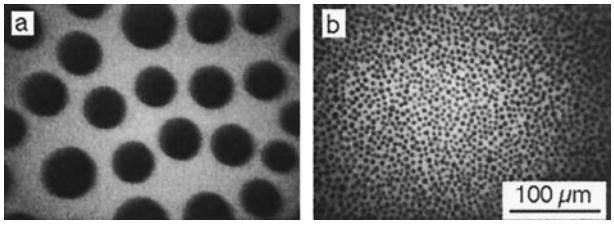

FIGURE 9 Fluorescence micrographs of a pure PA film (*a*) and a mixed PA/20 wt % SP-$B_{1–25}$ film (*b*) at 25°C on a buffered saline subphase. The images are taken at an area per PA molecule of 35 $Å^2$ (in the liquid-expanded/condensed coexistence region). Again the presence of the peptide disrupts the formation of large condensed-phase domains, resulting in a higher number density and smaller domain sizes.

packing of the lipid matrix, giving rise to a larger number of condensed domains with smaller individual domain size (see Fig. 9). At π = 30 mN/m, all the expanded phase has been converted to the condensed phase in pure PA monolayer, whereas the protein-enriched disordered phase persists in the mixed PA/SP-$B_{1–25}$ film, giving rise to the reduced scattering intensity found in GIXD data.

Collapsed structures

To examine the collapse structures in pure PA and in mixed lipid/peptide films, we compressed the monolayers on a pure water subphase at 16°C past collapse and carried out both GIXD and XR measurements. The GIXD measurements show several Bragg reflections (see Fig. 10) in the collapsed film and suggest that there is a coexistence between the monolayer at the air-water interface and patches of multilayers associated with the monolayer (see Figs. 11 and 13). Figs. 12, *a* and *b*, shows fluorescence images of the collapsed PA and mixed PA/20 wt % SP-$B_{1–25}$ films, respectively, which clearly show that the monolayer coexists

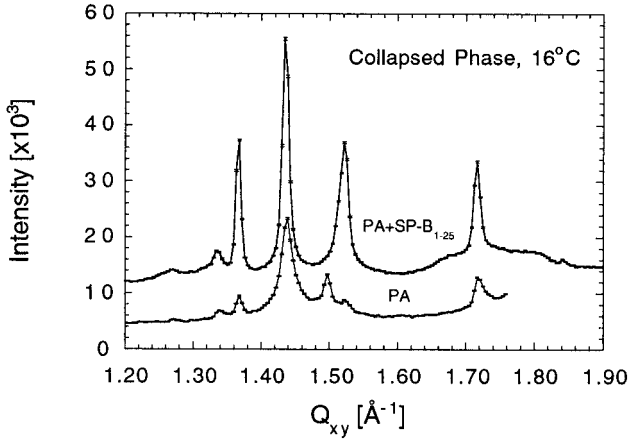

FIGURE 10 Bragg peaks from GIXD on pure water at 16°C of a pure PA film and a mixed PA/20 wt % SP-$B_{1–25}$ film, both taken after the films have collapsed. For clarity, the data for the mixed film have been offset vertically.

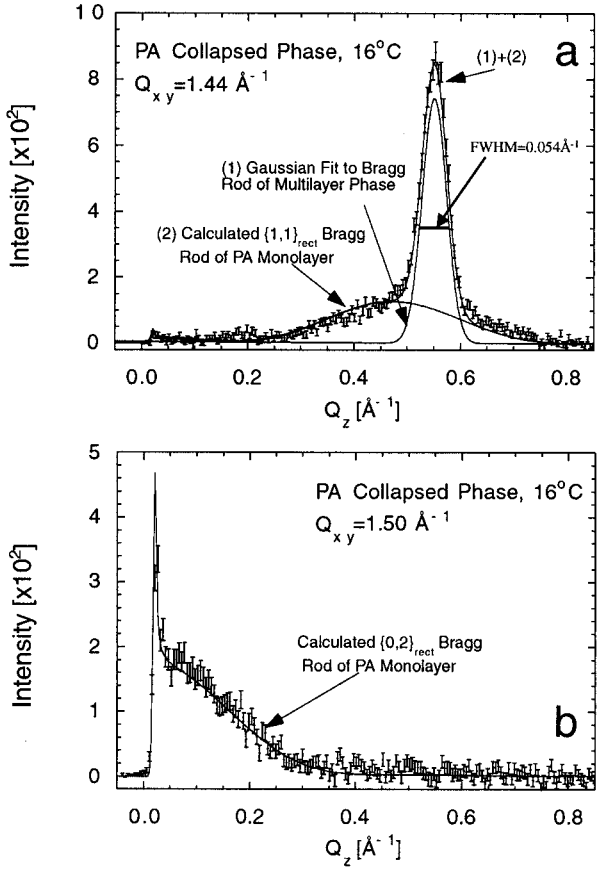

FIGURE 11 Bragg rod profiles for Q_{xy} = 1.44 $Å^{-1}$ (*a*), which corresponds to the $\{1,1\}_{rect}$ reflection, and Q_{xy} = 1.50 $Å^{-1}$ (*b*), which corresponds to the $\{0,2\}_{rect}$ reflection for a collapsed PA film on pure water at 16°C. Case *a* shows a coexistence between monolayer and multilayer structures; case *b* indicates only the presence of a monolayer.

with collapsed multilayer structures. The XR data, however, show gross deviations from the monolayer reflectivity curves obtained before collapse (see Fig. 15), rendering analysis impractical.

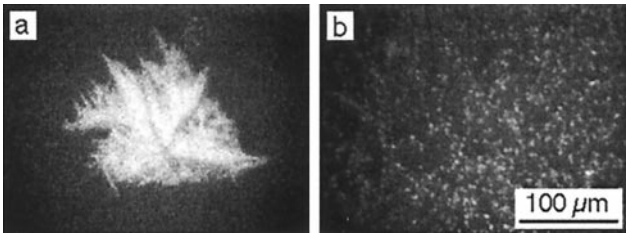

FIGURE 12 Fluorescence micrographs of collapsed pure PA (*a*) and mixed PA/SP-$B_{1–25}$ (*b*) films on pure water at 16°C. The presence of the protein has a drastic effect on the collapse mechanism and structure. In the absence of the protein, collapse occurs via heterogeneous nucleation, forming large multilayered collapsed structures. In the presence of the protein, collapse structures are much smaller in size but larger in number, suggesting a more homogeneous type of nucleation.

Grazing incidence x-ray diffraction on pure PA at 16°C on pure water (beyond monolayer collapse)

When the film was compressed past collapse, the surface pressure dropped to a value of 10 mN/m. Fig. 10 shows the GIXD patterns from this collapsed PA film. From the many Bragg peaks obtained, there are two, at $Q_{xy} = 1.44$ Å^{-1} and $Q_{xy} = 1.50$ Å^{-1}, that are similar to the $\{1,1\}_{rect}$ and $\{0,2\}_{rect}$ monolayer reflections, respectively, observed for the same system at 15 mN/m (see Fig. 3, *a* and *b*). By analyzing the background-subtracted Q_z intensity distribution of the resulting Bragg rods at $Q_{xy} = 1.44$ Å^{-1} and $Q_{xy} = 1.50$ Å^{-1}, we find that the latter Bragg rod gives a film thickness of ~20 Å (see Fig. 11 *b*), corresponding to a PA molecule tilted at 22°. The Bragg rod profile reflection at $Q_{xy} = 1.44$ Å^{-1} shows two overlapping peaks (see Fig. 11 *a*). The bottom profile can be fitted with ~20-Å slab of constant electron density that, once again, corresponds to the thickness of a PA monolayer. Therefore, the two Bragg rods correspond to $\{1,1\}_{rect}$ ($Q_{xy} = 1.44$ Å^{-1}) and $\{0,2\}_{rect}$ ($Q_{xy} = 1.50$ Å^{-1}) reflections of the PA monolayer. Fitting to the second, more intense intensity profile with a Gaussian function gives a full width at half-maximum of 0.054 Å^{-1}. This corresponds to a multilayer of ~116-Å thickness composed of approximately five PA monolayers. Our results indicate that upon collapse, the monolayer film relaxes to a lower surface pressure by building multilayer structures. This monolayer coexists with multilayers at the interface. Analysis of the Bragg peaks of the monolayer gives a structure with $d_{11} = 4.36$ Å and $d_{02} = 4.19$ Å, and the resulting rectangular unit cell has $|a| = 5.12$ Å and $|b| = 8.40$ Å. The area per molecule is 21.4 Å^2, and the molecular tilt is ~22.0°. These numbers are slightly larger than the 21.2-Å^2 unit area and the 21° tilt found at 15 mN/m, which should be expected as the final film pressure is only 10 mN/m. All the other Bragg peaks observed are from multilayer structures. Comparison of these peaks with 3D powder data will be presented below.

Grazing incidence x-ray diffraction on PA/20 wt % SP-B$_{1–25}$ at 16°C on pure water (beyond monolayer collapse)

When a mixed PA/SP-B$_{1–25}$ film was compressed past collapse, the film maintained a surface pressure of 25 mN/m. We find this post-collapse surface pressure for a mixed film is in general higher than that of a pure PA monolayer (~10 mN/m). GIXD measurements on a collapsed mixed film yielded a large number of Bragg peaks (see Fig. 10). We find two very similar Bragg peaks as with no SP-B$_{1–25}$ at $Q_{xy} = 1.44$ Å^{-1} and $Q_{xy} = 1.52$ Å^{-1}. By analyzing the background-subtracted Q_z intensity distribution of the Bragg rods, we find that the profile for $Q_{xy} = 1.44$ Å^{-1} (see Fig. 13 *a*) shows a total of three peaks, although none gives a monolayer film thickness. Hence,

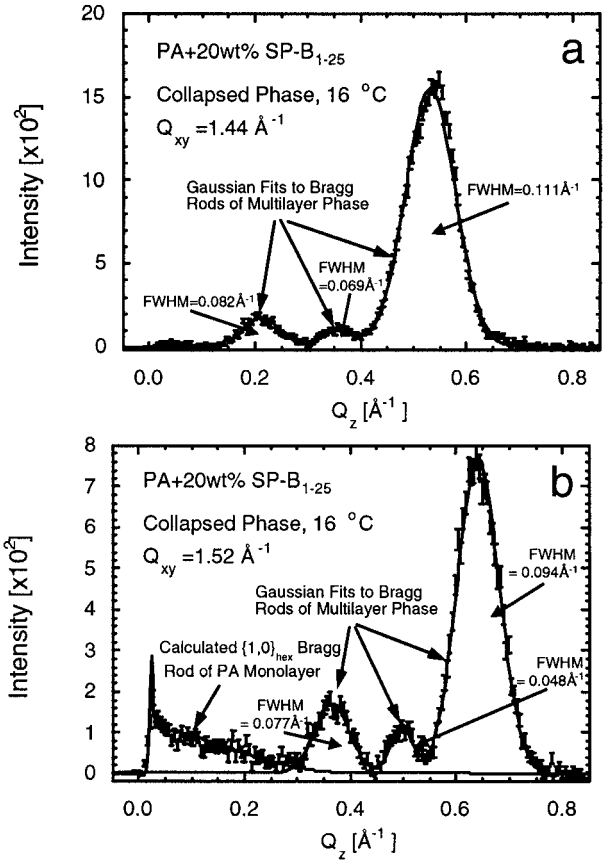

FIGURE 13 Bragg rod profiles for $Q_{xy} = 1.44$ Å^{-1} (*a*) and $Q_{xy} = 1.52$ Å^{-1} (*b*) for a collapsed PA/20 wt % SP-B$_{1–25}$ film on pure water at 16°C. Case *a* shows only multilayer structures; case *b* indicates the coexistence of monolayer and multilayer structures.

these reflections correspond to a multilayer structure. Fig. 13 *b* shows the Bragg rod profile of $Q_{xy} = 1.52$ Å^{-1}. Of the four peaks, the one with its maximum at $Q_z \sim 0$ Å^{-1} results from a film thickness of ~20 Å, whereas the others all indicate multilayer structures. Our results therefore point to the coexistence of a compressed, hexagonally packed monolayer film (only one $\{1,0\}_{hex}$ monolayer hexagonal reflection present) coexisting with multilayer structures at the interface. The presence of SP-B$_{1–25}$ in the film causes the monolayer to maintain the high-pressure untilted hexagonal lattice, with an intermolecular distance of 4.77 Å. The area per molecule is calculated to be 19.7 Å^2, which is similar to that of an uncollapsed PA monolayer with SP-B$_{1–25}$ at 40 mN/m. All the other Bragg peaks resulted from multilayers due to film collapse.

Comparison with 3D powder data

Fig. 14 shows the (Q_{xy}, Q_z) contour map of the Bragg peaks obtained in the collapsed film of PA/20 wt % SP-B$_{1–25}$ on pure water at 16°C. A similar contour map was also obtained for a collapsed pure PA film (not shown). In both

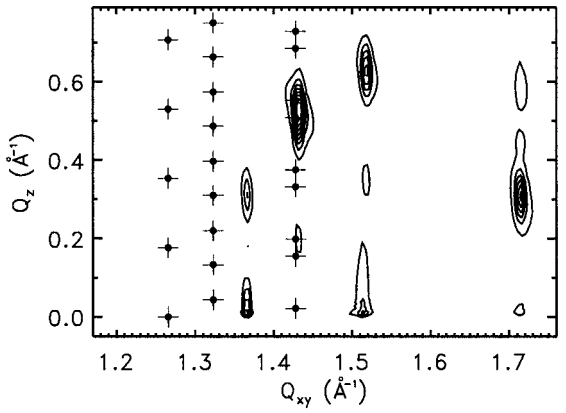

FIGURE 14 Contour map of the scattered intensity versus (Q_{xy}, Q_z) for a mixed PA/20 wt % SP-$B_{1–25}$ film after collapse on pure water at 16°C. Solid circles shown are (Q_{xy}, Q_z) positions of the calculated reflections extracted from 3D powder and single crystal results (Verma, 1955).

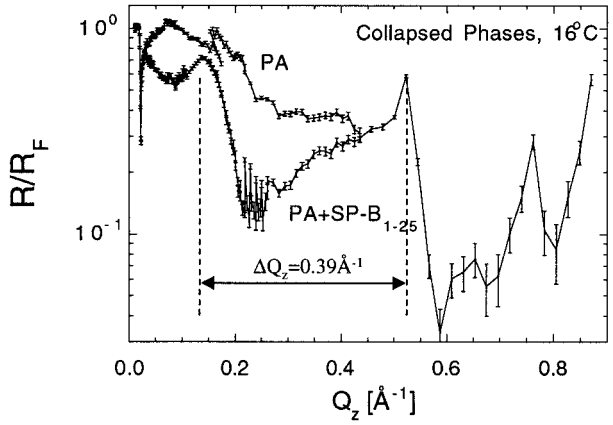

FIGURE 15 X-ray reflectivity curves for collapsed films of pure PA (*a*) and PA/20 wt % SP-$B_{1–25}$ (*b*) on pure water at 16°C.

cases, the GIXD data do not show the diffracted intensities stretched along Scherrer rings (loci of constant Q = sqrt((Q_{xy}^2 + Q_z^2)), but rather have well defined bumps that occur along Bragg rods (lines parallel to the Q_z vector). This indicates crystallite/multilayer structures with well-ordered, horizontal, basal planes. The observed positions of the maxima of the intensities do not correspond to the calculated (Q_{xy}, Q_z) values obtained from the known 3D crystal structures of palmitic acid (solid circles in Fig. 14). (In the calculation, the normal to the basal plane of the C-polymorph reported by Verma (1955) was oriented parallel to the Q_z axis; the lattice constants more recently reported in entry 24–1853, Powder Diffraction File, International Center for Diffraction Data (http://www.icdd.com/) by Li (1972) were used.) However, the positions of the (Q_{xy}, Q_z) intensity maxima of the collapsed PA as well as the PA/20 wt % SP-$B_{1–25}$ are identical (except for those coming from the monolayer). The identity of the positions of the intensity maxima obtained in the presence or absence of the peptide suggest that the ordered phase within the collapse structure does not contain SP-$B_{1–25}$ molecules.

X-ray reflectivity

The reflectivity curves for PA and PA/20 wt % SP-$B_{1–25}$ collapsed films on pure water at 16°C are shown in Fig. 15. Comparing these figures with those in Fig. 5 clearly demonstrate the added complexity when multilayer structures are present, making them difficult to analyze using simple slab models. Fig. 15 shows a peak at Q_z = 0.14 Å^{-1}, another one at Q_z = 0.53 Å^{-1}, and probably yet another one at ~0.9 Å^{-1}. The difference in the Q_z value between the first and the second peak is 0.39 Å^{-1}; a rough estimation gives a repeat distance of 16.5 Å ($2\pi/\Delta Q_z$), which probably corresponds to an interlayer spacing {0,0,*l*}. However, it should be stressed that this is merely a rough estimate.

DISCUSSION

GIXD and XR measurements were used to investigate the influence of the truncated LS peptide, SP-$B_{1–25}$, on the packing of PA monolayers at the air-water interface. From the GIXD we infer that on both pure water and buffered saline subphases, the peptide is incorporated into the disordered phase of the PA monolayer. The insertion of the peptide leads to a reduced amount of ordered phase in the film, as reflected by a decrease in scattering intensity in our GIXD data. This reduction in scattering intensity is particularly apparent on a pure water subphase at 16°C. Below the triple point of the PA film, a disordered phase does not exist at non-zero surface pressures in pure PA films; the disordered phase that occurs when peptide is present points to the fluidizing capabilities of SP-$B_{1–25}$. This finding corroborates our fluorescence microscopy data, which show that a disordered phase is created when SP-$B_{1–25}$ is present in the PA monolayer (Lipp et al., 1996, 1997).

Although SP-$B_{1–25}$ induces a disordered phase in the monolayer, our GIXD data show that the peptide does not affect the molecular packing of the ordered phase. Within experimental errors, films with and without SP-$B_{1–25}$ have identical packing parameters. This suggests that the peptide is completely excluded from the ordered phase of the film and hence must reside in the disordered portion of the monolayer. It should be pointed out that the lattice parameters obtained here for PA and the mixed PA/SP-$B_{1–25}$ monolayers are similar to those found in longer-chain fatty acids (Kuzmenko et al., 1998). The lattice parameters and structures obtained here for PA and the mixed PA/SP-$B_{1–25}$ monolayers are in line with the systematics found in longer-chain fatty acids: roughly, the same phase diagram, with the same structures, applies to all members of the homologous series, with shorter molecules being equivalent to higher temperatures (Bibo and Peterson, 1990; Kaganer et al., 1999). The phase sequence from *L2* to *LS* (superliquid)

packing upon increasing surface pressure is typical (Kaganer et al., 1999). The shorter correlation lengths along the tilt direction found here are also common to *L2* phases.

The XR data yielded drastic differences between the reflectivity curve of the pure PA film and the mixed PA/SP-$B_{1–25}$ film. Using slab models to analyze our data, we were able to fit the pure PA monolayer with only two boxes (for the head region and the tail region). However, the mixed PA/SP-$B_{1–25}$ case required a four-box model to obtain a comparable fit. The mixed monolayer has a total film thickness of 29.2 Å, which is considerably thicker than even an untilted PA film. This shows that the peptide is associated with the lipid monolayer at the air-water interface, and that portion of it is protruding into the subphase. Based on the dimensions of SP-$B_{1–25}$ obtained via molecular dynamic simulation (Gordon et al., 2000), the angle of insertion of the peptide is ~56° relative to the interface normal. We have also carried out reflectivity measurements on phospholipid and phospholipid/SP-$B_{1–25}$ systems. However, large headgroups of phospholipids (DPPC, DPPG, and POPG) render it difficult to deduce the angle of insertion of the peptide into phospholipid films (unpublished data). It is important to note that XR measurements are sensitive to both the ordered and the disordered phase. Hence, the electron density distribution used for our analysis represents lateral averaging over both the ordered and disordered portions of the monolayer. This results in a larger area, of 25.3 Å, than those obtained from GIXD measurements (which is sensitive only to the ordered phase) under similar conditions.

GIXD and XR data on collapsed films show a large number of Bragg peaks and complicated reflectivity curves. For pure PA, analysis of two of the Bragg rods at Q_{xy} = 1.44 $Å^{-1}$ and Q_{xy} = 1.50 $Å^{-1}$, show that the underlying monolayer has tilted structure based on a rectangular unit cell. The monolayer is similar in structure to the uncollapsed monolayer at 15 mN/m. All other Bragg peaks result from scattering from multilayer structures. In the mixed PA/SP-$B_{1–25}$ case, an analogous analysis of the collapsed film yields, for the monolayer phase, an untilted hexagonal lattice similar to that found in an uncollapsed mixed monolayer at 40 mN/m. In the absence of the peptide, the monolayer phase of the collapsed film relaxes to a lower surface pressure and hence to a more relaxed packing configuration as compared with that of a mixed PA/SP-$B_{1–25}$ film. The (Q_{xy}, Q_z) positions of the intensity maxima from the multilayer collapsed structures in both the pure PA film and the mixed film are superimposable, suggesting that the multilayer collapsed structures are highly enriched in PA.

Our findings that both the condensed phase as well as the collapse phase are essentially free of peptide suggest that the change in monolayer collapse is due to changes in the global, or micron-scale, morphology rather than the local, or molecular-scale, structure. The change from heterogeneously distributed, large collapse structures (Fig. 12 *a*) to more uniformly distributed, small collapse structures (Fig. 12 *b*) is due to the physical isolation and reduction in size of the condensed-phase domains (see Fig. 9) rather than by specific chemical or physical inhibition by the peptide. These results confirm an earlier speculation by some of us (Lipp et al., 1996) that the identical solid phase of PA is collapsing with and without the peptide; the change in the morphology and surface pressure at collapse is due to a conversion between heterogeneous and homogeneous nucleation, in the absence and the presence of the peptide, respectively. Nucleation of the three-dimensional collapse structures must occur within each small solid-phase domain in the presence of the peptide, and the collapse structure can propagate only within the domain in which it is nucleated. Moreover, the probability of a heterogeneous nucleation site within a particular small domain is small, resulting in homogeneous nucleation of collapse. This leads to the smaller collapse structures and the higher surface pressure at collapse. If the solid phase is continuous, a limited number of defects can act as sites for heterogeneous nucleation and lead to large collapse structures that can spread across the entire monolayer.

APPENDIX

Fitting of the x-ray reflectivity data using coherent and incoherent averaging

The four-box model presented in the text is a fit based on the assumption that the PA/SP-B mixed monolayer forms a homogeneous thin film at the air-water interface. In this case we treat reflectivity kinematically using the so-called master formula for reflectivity:

$$R(q_z) = R_F(q_z)\,(\rho_{Sub})^{-2}\left|\int (d\rho(z)/dz)\,\exp(iq_z z)\,dz\right|^2 \quad (1)$$

The interpretation of the reflectivity data from a heterogeneous monomolecular layer may be more difficult if the size of the differently reflecting domains exceeds the coherence length of the x-ray beam. Consider, for example, a surface with a random distribution of two types of domains (as in the case of a mixed PA/SP-B monolayer), differing in reflectivity, say, $R_1(q_z) = |\,r_1(q_z)\,|^2$ and $R_2(q_z) = |\,r_2(q_z)\,|^2$, where $r_i(q_z)$ is a complex function describing the reflectance of each domain (cf. Eq. 1). If each set of domains is macroscopically large and homogeneous, one would expect each set to reflect x-rays independent of each other, and thus the measured reflectivity should be the (incoherent) average of the intensities:

$$\begin{aligned} R(q_z) &= \Psi\,R_1(q_z) + (1-\Psi)\,R_2(q_z) \\ &= \Psi|r_1(q_z)|^2 + (1-\Psi)|r_2(q_z)|^2 \end{aligned} \quad (2)$$

with ψ being the fraction of the total area occupied by constituent 1.

We tried to fit our reflectivity data using Eq. 2 and we designed several simple box models to describe the mixed monolayer structure.

Two boxes for the pure PA domain and two boxes for the mixed PA/SP-B domain, respectively

We find that this model does not work (with fixed or released fitting parameters for the PA part) as it either gives high χ^2 values and chemically

unreasonable values for parameters depicting the PA tail region (number of electrons, $\#e^-_{tail} = 87$; thickness, $t_{tail} = 18.2$ Å; area per molecule, $A_{mol} = 28.9$ Å^2), or drives the concentration of PA to values close to zero (when PA parameters are fixed) and the parameters of the PA/SP-B part to the following values: $\#e^-_1 = 145$, $t_1 = 13.1$ Å, $\#e^-_2 = 121$, $t_2 = 13.6$ Å, $A_{mol} = 30.4$ Å^2, $\sigma = 2.4$ Å.

Two boxes for the pure PA domain and three boxes to describe the mixed PA/SP-B domain

A reasonable fit was achieved only for the mole fraction of PA, $\psi = 0.27$, and the following set of parameters: PA portion with $\#e^-_{head} = 19.6$, $t_{head} = 1.4$ Å, $\#e^-_{tail} = 121$, $t_1 = 15.2$ Å (value too small), $A_{mol} = 22.7$ Å^2; PA/SP-B portion with $\#e^-_1 = 145$, $t_1 = 11.2$ Å, $\#e^-_2 = 34$, $t_2 = 2.54$ Å, $\#e^-_3 = 131$, $t_3 = 14.9$ Å, $A_{mol} = 34.7$ Å^2, $\sigma = 2.5$ Å. Moreover, the obtained ψ contradicts with the coverage of PA as observed by fluorescence microscopy (~0.8). Fixing ψ to the value of 0.8 makes the fit much worse.

Two boxes for the pure PA domain and four boxes for the mixed PA/SP-B domain, respectively

Our first approach was to fix the parameters of the PA portion ($\#e^-_{head} = 24$, $t_{head} = 2.2$ Å, $\#e^-_{tail} = 121$, $t_1 = 18.6$ Å, $A_{mol} = 18$ Å^2) and fit only the PA/SP-B part of the monolayer. In this case, the fitting program converged to a mole fraction of PA, ψ, close to zero and the value of the rest of the parameters very close to the values obtained using the four-box model presented in the text ($\#e^-_1 = 84$, $t_1 = 9.46$ Å, $\#e^-_2 = 25.5$, $t_2 = 2.44$ Å, $\#e^-_3 = 43.5$, $t_3 = 5.3$ Å, $\#e^-_4 = 84$, $t_4 = 11.5$ Å, $A_{mol} = 25.1$ Å^2, $\sigma = 2.3$ Å).

When all fitting parameters were allowed to run freely (except for the number of electrons in the hydrocarbon tail of PA), we obtained the following set of values for our fitting parameters: PA portion with $\psi = 0.48$ (value too small), $\#e^-_{head} = 18.8$, $t_{head} = 1.25$ Å, $\#e^-_{tail} = 121$, $t_{head} = 15.4$ Å (again value too small), $A_{mol} = 24.6$ Å^2 (value too big), and PA/SP-B portion with $\#e^-_1 = 79$, $t_1 = 5.8$ Å, $\#e^-_2 = 63.5$, $t_2 = 4.5$ Å, $\#e^-_3 = 30$, $t_3 = 2.36$ Å, $\#e^-_4 = 125$, $t_4 = 15.2$ Å, $A_{mol} = 34.8$ Å^2, $\sigma = 2.57$ Å.

Fixing $\#e^-_{head}$ for PA to 22, A_{mol} to 18 Å^2 together, and $\#e^-_{tail}$ to 121 results in another set of fit parameters with an unreasonably low PA mole fraction of $\psi = 0.18$.

In summary, using the incoherent reflectivity refinement it is impossible to achieve surface fraction of PA larger than 48%. The value of ψ becomes even smaller (~20%) when we restrict the fitting parameters for the PA portion to chemically reasonable values.

For a macroscopically homogeneous mixture of two constituents occupying the whole water surface, conversely, the total electron density locally is the sum of contributions from each of the constituents:

$$\rho(z) = \varphi\rho_1(z) + (1 - \varphi)\,\rho_2(z), \tag{3}$$

with φ being the fraction of constituent 1 present. Substitution of Eq. 3 into Eq. 1 yields the average of the amplitudes, i.e., the coherently averaged reflectivity:

$$R(q_z) = |\varphi\, r_1(q_z) + (1 - \varphi)\, r_2(q_z)|^2 \tag{4}$$

We have used similar fitting models as described above to check the validity of treating the reflectivity data as a coherent case, whereby the structure of the pure PA domain was described by two boxes whereas the mixed PA/SP-B structure was characterized by two, three, or four boxes, respectively. Table 2 shows the fitting parameters for several of these models; the subscript *f* indicates that the parameter was kept fixed during the refinement.

Although the results of the coherent reflectivity refinement are not conclusive regarding the structure of the PA/SP-B domain, several observations can be made from Table 2. First, the surface area fraction of PA is always converging to the values between 0.74 and 0.83, in good agreement with that observed using fluorescence microscopy. Second, all of the presented models have certain deficiencies: they give lower than expected lengths of the fully stretched PA hydrocarbon tail (15 × 1.26 = 18.9 Å) in

TABLE 2 Fitting parameters for various models used for XR data on pure water at 16°C

		Palmitic acid						Palmitic acid with SP-B$_{1-25}$											
		Conc φ	A_{mol} (Å^2)	$\#e^-_{head}$	t_{head} (Å)	$\#e^-_{tail}$	t_{tail} (Å)	A_{mol} (Å^2)	$\#e^-_1$	t_1 (Å)	$\#e^-_2$	t_2 (Å)	$\#e^-_3$	t_3 (Å)	$\#e^-_4$	t_4 (Å)	σ (Å)	χ^2
1	2box + 2box	0.76	19_f	22_f (1.73)	2.0$_f$	121_f (1.15)	16.6	68.9	163 (1.56)	4.54	81 (0.39)	9.0					2.36	256
2	2box + 3box	0.79	19_f	22_f (2.53)	1.37	121_f (1.11)	17.2	47.6	125 (0.925)	8.5	115 (2.07)	3.5	22 (0.12)	11.6			2.53	255
3	2box + 4box	0.75	19_f	22_f (2.18)	1.59	121_f (1.14)	16.7	48.5	90 (1.32)	4.22	24.4 (1.03)	1.47	55.3 (1.67)	2.05	34 (0.2)	10.4	2.34	260
4	2box + 4box	0.83	24 19_f	2.0 (1.89)	121_f	18.4 (1.04)		80 29.8	8.8 (0.91)	23.6	2.07 (1.15)	53.4	3.15 (1.7)	63	14.8 (0.43)		2.35	275
5	2box + 4box	0.74	19_f	22_f (2.17)	1.6	121_f (1.1)	17.3	50.5	202 (2.72)	4.4	84.4 (3.05)	1.64	59 (1.49)	2.35	14.4 (0.08)	11	2.52	166
6	2box + 4box	0.74	19_f	29.8 (2.03)	2.31	121_f (1.17)	16.3	26.1	84 (0.95)	10.2	35 (1.22)	3.3	47 (1.71)	3.15	9 (0.09)	11.3	2.46	255

Values in parentheses indicate electron densities normalized by electron density of the water subphase ($0.334e^-/$Å^3).

cases 1, 2, 3, 5, and 6; they result in boxes with electron densities for the PA/SP-B portion of the monolayer lower than that of water (cases 4 and 6); and case 3 results in unexpected dips in the electron density distribution for the PA/SP-B portion.

Although case 5 has the smallest χ^2 value, only case 6 reproduces nicely the small dip in the reflectivity curve around $Q = 0.43$ Å^{-1} or $20 \times Q_c$.

In conclusion, contrary to what would be expected from comparison of the coherence length of the beam (which, in the case of our experiments, is between 1 and 6 μm depending on the angle of incidence) with the typical size of PA or PA/SP-B domains as observed by fluorescence microscopy, the incoherent reflectivity treatment does not work as well as the coherent one. Because x-ray reflectivity measures smaller length scales than fluorescence microscopy, the discrepancy can be explained by the presence of other non-crystalline microscopic domains of different structures. The incoherent (or coherent) average applies when the domains are much larger (or much smaller) than the coherence area of the reflectivity experiment. The coherence area depends on the Q-resolution and is typically of the order of microns along the x-ray beam direction by tens of nanometers in the perpendicular direction. In either case, however, the reflectivity is an average over the entire surface.

We gratefully acknowledge beam time at HASYLAB at DESY, Hamburg, Germany, and funding by the programs DanSync (Denmark) and TMR of the European Community (contract ERBFMGECT950059). We thank Dr. Rita Hazal for a useful discussion and Dr. Mark Sherman of Beckman-The City of Hope Molecular Modeling Core Facility (Cancer Center Support grant P30 CA33572) for his assistance with the modeling of the SP-B$_{1-25}$ peptide at the palmitic acid monolayer. K.Y.C.L. is grateful for the support from the Camille and Henry Dreyfus New Faculty Award (NF-98–048), the March of Dimes Basil O'Connor Starter Scholar Research Award (5-FY98–0728), the American Lung Association (RG-085-N), and the David and Lucile Packard Foundation (99–1465). A.G. is supported by the Searle Scholars Program/the Chicago Community Trust (99-C-105). J.A.Z. and M.M.L. were supported by National Institutes of Health Grant HL51177. A.J.W. was supported by National Institutes of Health Grant HL55534. The Manuel Lujan Jr., Neutron Scattering Center is a national user facility funded by the United States Department of Energy, Office of Basic Energy Sciences - Materials Science, under contract number W-7405-ENG-36 with the University of California. This work was also supported in part by the MRSEC Program of the National Science Foundation under Award Numbers DMR-9808595 (The University of Chicago) and DMR96–32716 (University of California, Santa Barbara).

REFERENCES

Als-Nielsen, J., D. Jacquemain, K. Kjaer, F. Leveiller, M. Lahav, and L. Leiserowitz. 1994. Principles and applications of grazing incidence X-ray and neutron scattering from ordered molecular monolayers at the air-water interface. *Phys. Rep.* 246:251–313.

Als-Nielsen, J., and K. Kjaer. 1989. X-ray reflectivity and diffraction studies of liquid surfaces and surfactant monolayers. *In* Phase Transitions in Soft Condensed Matter. T. Riste and D. Sherrington, editors. Plenum Press, New York.113–138.

Bibo, A., and I. Peterson. 1990. Phase diagram of monolayers of the long chain fatty acids. *Adv. Materials.* 2:309–311.

Cockshutt, A., D. Absolom, and F. Possmayer. 1991. The role of palmitic acid in pulmonary surfactant: Enhancement of surface activity and prevention of inhibition by blood proteins. *Biochim. Biophys. Acta.* 1085:248–256.

Egbert, J., H. Sloot, and A. Mazure. 1989. Minimal surface tension, squeeze-out and transition temperatures of binary mixtures of dipalmitoylphosphatidylcholine and unsaturated phospholipids. *Biochim. Biophys. Acta.* 1002:109–113.

Eisenberger, P., and W. C. Marra. 1981. X-ray diffraction study of the Ge (001) reconstructed surface. *Phys. Rev. Lett.* 46:1081.

Frahm, R., J. Weigelt, G. Meyer, and G. Materlik. 1995. X-ray undulator beamline BW1 at DORIS III. *Rev. Sci. Instrum.* 66:1677–1680.

Gordon, L. M., S. Horvath, M. Longo, J. A. Zasadzinski, H. W. Taeusch, K. Faull, C. Leung, and A. J. Waring. 1996. Conformation and molecular topography of the N-terminal segment of surfactant protein B in structure-promoting environments. *Protein Sci.* 5:1662–1675.

Gordon, L. M., K. Y. C. Lee, M. M. Lipp, J. A. Zasadzinski, F. J. Walther, M. A. Sherman, and A. J. Waring. 2000. Conformational mapping of the N-terminal segment of surfactant protein B (SP-B) in lipid 13C-enhanced Fourier transform infrared spectroscopy. *J. Peptide Res.* 55: 330–347.

Hall, S., A. Venkitaraman, J. Whitsett, B. Holm, and R. Notter. 1992. Importance of hydrophobic apoproteins as constituents of clinical exogenous surfactants. *Am. Rev. Respir. Dis.* 145:24–30.

Hawgood, S., M. Derrick, and F. Poulain. 1998. Structure and properties of surfactant protein B. *Biochim. Biophys. Acta.* 1408:150–160.

Jacquemain, D., F. Leveiller, S. Weinbach, M. Lahav, L. Leiserowitz, K. Kjaer, and J. Als-Nielsen. 1991. Crystal-structures of self-aggregates of insoluble aliphatic amphiphilic molecules at the air-water interface: an x-ray synchrotron study. *J. Am. Chem. Soc.* 113:7684.

Johansson, J., and T. Curstedt. 1997. Molecular structures and interactions of pulmonary surfactant components. *Eur. J. Biochem.* 244:675–693.

Kaganer, V. M., H. Möhwald, and P. Dutta. 1999. Structure and phase transitions in Langmuir monolayers. *Rev. Modern Phys.* 71:779–819.

Kenn, R. M., C. Böhm, A. M. Bibo, I. R. Peterson, H. Möhwald, J. Als-Nielsen, and K. Kjaer. 1991. Mesophase and crystalline phases in fatty-acid monolayers. *J. Phys. Chem.* 95:2092–2097.

Keough, K. 1985. Lipid Fluidity and Respiratory Distress Syndrome. Elsevier, Amsterdam.

Kjaer, K. 1994. Some simple ideas on x-ray reflection and grazing-incidence diffraction from thin surfactant films. *Physica B.* 198: 100–109.

Kjaer, K., J. Als-Nielsen, C. A. Helm, P. Tippman-Krayer, and H. Möhwald. 206. 1989. Synchrotron x-ray diffraction and reflection studies of arachidic acid monolayers at the air-water interface. *J. Phys. Chem.* 93:3200–3203.

Kuzmenko, I., V. M. Kaganer, and L. Leiserowitz. 1998. Packing of hydrocarbon chains and symmetry of condensed phases in Langmuir monolayers. *Langmuir.* 14:3882–3888.

Lee, K. Y. C., M. M. Lipp, J. A. Zasadzinski, and A. J. Waring. 1997. Morphological effects of full length SP-B protein and shorter model peptide on lipid monolayers at the air-water interface. *Colloids Surfaces A.* 28:225–242.

Lin, B., M. C. Shih, T. M. Bohanon, G. E. Ice, and P. Dutta. 1990. Phase-diagram of a lipid monolayer on the surface of water. *Phys. Rev. Lett.* 65:191–194.

Lipp, M. M., K. Y. C. Lee, D. Y. Takamoto, J. A. Zasadzinski, and A. J. Waring. 1998. Coexistence of buckled and flat monolayers. *Phys. Rev. Lett.* 81:1650–1653.

Lipp, M. M., K. Y. C. Lee, J. A. Zasadzinski, and A. J. Waring. 1996. Phase and morphology changes induced by SP-B protein and its amino-terminal peptide in lipid monolayers. *Science.* 273:1196–1199.

Lipp, M. M., K. Y. C. Lee, J. A. Zasadzinski, and A. J. Waring. 1997. Fluorescence, polarized fluorescence, and Brewster angle microscopy of palmitic acid and lung sufactant protein B monolayers. *Biophys. J.* 72:2783–2804.

Longo, M., A. Waring, and J. Zasadzinski. 1992. Lipid bilayer surface association of lung surfactant protein SP-B, amphipathic segment detected by flow immunofluorescence. *Biophys. J.* 63:760–773.

Majewski, J., R. Popovitz-Biro, W. Bouwman, K. Kjaer, J. Als-Nielsen, M. Lahav, and L. Leiserowitz. 1995. The structural properties of uncompressed crystalline monolayers of alcohols CnH2n+1OH (n = 13–31) on water and their role as ice nucleator. *Chem. Eur. J.* 1:302–309.

Mathialagan, N., and F. Possmayer. 1990. Low-molecular weight hydrophobic proteins from bovine pulmonary surfactant. *Biochim. Biophys. Acta.* 1045:121–127.

Mizuno, K., M. Ikegami, C. M. Chem, T. Ueda, and A. H. Jobe. 1995. Surfactant protein B supplementation improves in vivo function of a modified natural surfactant. *Pediatr. Res.* 35:271–276.

Pastrana-Rios, B., C. Flach, J. Brauner, A. Mautone, and R. Mendelsohn. 1994. A direct test of the "squeeze-out" hypothesis of lung surfactant function: external reflection FT-IR at the air-water interface. *Biochemistry.* 33:5121–5127.

Possmayer, F. 1988. A proposed nomenclature for pulmonary surfactant-associated proteins. *Am. Rev. Respir. Dis.* 138:990–998.

Shapiro, D. L., and R. H. Notter. 1989. Surfactant Replacement Therapy. Alan R. Liss, New York.

Takahashi, A., A. J. Waring, J. Amirkhanian, B. Fan, and H. W. Taeusch. 1990. Structure-function relationship of bovine pulmonary surfactant proteins: SP-B and SP-C. *Biochim. Biophys. Acta.* 1044:43–49.

Tokieda, K., J. A. Whitsett, J. C. Clark, T. E. Weaver, K. Ikeda, K. B. McConnell, A. H. Jobe, M. Ikegami, and H. S. Iwamoto. 1997. Pulmonary dysfunction in neonatal SP-B deficient mice. *Am. J. Physiol.* 273:L875–L882.

Veldhuizen, R., K. Nag, S. Orgeig, and F. Possmayer. 1998. The role of lipids in pulmonary surfactant. *Biochim. Biophys. Acta.* 1408:90–108.

Verma, A. J. 1955. Interferometric and x-ray investigation of the growth of long-chain fatty acid crystals. *Proc. Roy. Soc. A.* 228:34–50.

Walther, F. J., J. Hernandez-Juviel, R. Bruni, and A. J. Waring. 1997. Spiking Survanta with synthetic surfactant peptides improves oxygenation in surfactant deficient rats. *Am. J. Respir. Crit. Care Med.* 156: 855–861.

Walther, F. J., J. Hernandez-Juviel, R. Bruni, and A. J. Waring. 1998. Protein composition of synthetic surfactant affects gas exchange in surfactant deficient rats. *Pediatr. Res..* 43:666–673.

Waring, A., W. Taeusch, R. Bruni, J. Amirkhanian, B. Fan, R. Stevens, and J. Young. 1989. Synthetic amphipathic sequences of surfactant protein-B mimic several physiochemical and in vivo properties of native pulmonary surfactant proteins. *Peptide Res.* 2:308–313.

Weissbuch, I., R. Biro-Popovitz, M. Lahav, L. Leiserowitz, K. Kjaer, and J. Als-Nielsen. 1997. Molecular self assembly into crystals at air-liquid interfaces. *In* Advances in Chemical Physics. I. Prigogine and S. A. Rice, editors. Wiley, New York. 39–120.